



## **Final Draft** **of the original manuscript**

Riaz, A.; Witte, K.; Bodnar, W.; Hantusch, M.; Schell, N.; Springer, A.;  
Burkel, E.:

**Structural changes and pseudo-piezoelectric behaviour of  
field assisted sintered calcium titanate.**

In: Materialia. Vol. 15 (2021) 100998.

First published online by Elsevier: 05.01.2021

<https://dx.doi.org/10.1016/j.mtla.2021.100998>

# Structural changes and pseudo-piezoelectric behaviour of field assisted sintered calcium titanate

Abdullah Riaz<sup>a,\*</sup>, Kerstin Witte<sup>b</sup>, Wiktor Bodnar<sup>b</sup>, Martin Hantusch<sup>c</sup>, Norbert Schell<sup>d</sup>, Armin Springer<sup>e</sup>, Eberhard Burkelf<sup>f</sup>

<sup>a</sup>University of Rostock, Microfluidics, Faculty of Mechanical Engineering and Marine Technology, Justus-von-Liebig-Weg 6, 18059 Rostock, Germany

<sup>b</sup>INP Leibniz Institute for Plasma Science and Technology, Felix-Hausdorff-Str. 2, 17489 Greifswald, Germany

<sup>c</sup>IFW Dresden, Helmholtz-Str. 20, 01069 Dresden, Germany

<sup>d</sup>Helmholtz-Zentrum Geesthacht, Max Planck-Str. 1, 21502 Geesthacht, Germany

<sup>e</sup>University Medical Center Rostock, Medical Biology and Electron Microscopy Centre, Strempel-Str. 14, 18057 Rostock, Germany

<sup>f</sup>University of Rostock, Institute of Physics, Albert Einstein-Str. 23-24, 18059 Rostock, Germany

\*Corresponding author: E-mail address: [abdullah.riaz@uni-rostock.de](mailto:abdullah.riaz@uni-rostock.de)

## Abstract

The polycrystalline perovskite calcium titanate has an orthorhombic crystal structure at room temperature, which belongs to a centro-symmetric point group. Due to this fact, it does not show piezoelectric behaviour. However, such behaviour is observed in nanostructured calcium titanate prepared by sol-gel synthesis and field assisted sintering. Whereas, the conventionally sintered sample does not show this behaviour. Presumably, the instability of regular  $\text{TiO}_6$  octahedra results in the off-centering of titanium positions of the field assisted sintered calcium titanate. This phenomenon leads to the generation of electric dipoles due to the lattice distortion produced by the formation of highly localized defects, i.e. oxygen vacancies, during densification by the field assisted sintering. As a result, pseudo-piezoelectric behaviour is observed, which confirms that the field assisted sintering triggers the piezoelectric effect but not the conventional sintering. The charge ( $Q$ ) produced in the field assisted sintered sample and the piezoelectric constant ( $d_{33}^*$ ) values have been determined to be  $Q = (2.1 \pm 0.3) \text{ pC}$  and  $d_{33+}^* \sim (7.13 \pm 0.4) \text{ pm/V}$  or  $d_{33-}^* \sim (-5.95 \pm 0.3) \text{ pm/V}$ , respectively. This particular response of nanostructured calcium titanate is of great interest in biomedicine because it can improve the osseointegration of an implant.

**Keywords:** Calcium titanate ( $\text{CaTiO}_3$ ); FAST sintering; piezoelectric effect; distorted structure; biomaterials

## 1. Introduction

During the past years, research and development of orthopaedic implant materials were focused on titanium and its alloys because of their low elastic modulus, high corrosion resistance, good biocompatibility and low density [1, 2]. However, these materials have poor tribological properties and lack of bioactive functionality [3]. Nowadays, the primary challenge in orthopaedic implant material development is the improvement of osseointegration. As bone has notable electrical and piezoelectric properties, an implant material with comparable properties can be used to mimic natural bone which can help in the healing process [4-6]. Therefore, there is a great interest in piezoelectric ceramics because upon deformation due to mechanical stresses, they can facilitate cell-material interaction without using an external source.

In general, the human mesenchymal stem cells can be induced to differentiate into osteoblasts by the piezoelectric materials. The osteoblasts produce bone matrix proteins and mineralize the matrix into bones [7]. It has been reported that *in-vivo* implantation of piezoelectric materials has promoted encouraging results in repairing nerve injuries, bone formation and wound healing [8]. Other studies showed that the *in-vitro* results have positive effects, such as differentiation of Sprague-Dawley rat's osteoblasts on ceramics. It also showed better attachment and proliferation on the charged surface of the poled ceramics than unpolarized surface [9]. Nevertheless, most of the commonly known ceramics, e.g. lead titanate, zirconate titanate or their compounds, are toxic, which can exhibit ion dissolution in biological fluids [10-12].

Previous experiments on surface modifications of titanium with perovskite calcium titanate ( $\text{CaTiO}_3$ ) ceramics revealed that it improves bone binding strength and that it is also a non-toxic compound [13-15]. However, it does not exhibit piezoelectric behaviour. The crystal structure of  $\text{CaTiO}_3$  consists of corner linked  $\text{TiO}_6$  octahedra with calcium atoms allocated between the octahedra. It has an orthorhombic crystal structure at room temperature, which belongs to a centro-symmetric point group, i.e. mmm [16, 17]. Ceramics can only show piezoelectric behaviour if they have electric dipoles which are produced due to non-symmetrical charge distribution in the lattice, like other perovskite titanates as lead titanate, strontium titanate or barium titanate [11, 18, 19]. However, it is predicted that the instability of regular  $\text{TiO}_6$  octahedra will result in the off-centering of the titanium positions in  $\text{CaTiO}_3$  which break the crystal symmetry causing the generation of electric dipoles [20]. This off-centering of titanium atoms was first observed by aberration-corrected TEM imaging in a twin boundary of  $\text{CaTiO}_3$  single crystal grown by the floating zone technique [21]. However, the fundamental challenge is to create instability of regular  $\text{TiO}_6$  octahedra in bulk polycrystalline  $\text{CaTiO}_3$ , which could lead to a piezoelectric response of the bulk. One possibility to generate such distortions in the crystal lattice is the production of lattice oxygen defects. For example, defects are acceptor-oxygen-vacancy dipoles. These electrically charged defects or in other words electric dipoles can be created by a thermal treatment in an oxygen poor atmosphere at elevated temperature [22]. However, the migration of defects into their equilibrium configuration should be prevented. If the ceramics are rapidly cooled from elevated temperature, a freezing of the distribution of defects could be achieved. It is suggested that the freezing of the distribution of such electrically charged defects can strongly influence the ferroelectric and piezoelectric properties [23]. Consequently, it should be possible to manipulate the crystal structure of  $\text{CaTiO}_3$  in order to trigger a

piezoelectric behaviour. A promising technique for producing such materials is the field assisted sintering technique (FAST) [24]. Recently, it is reported that FAST sintered nanostructured  $\text{CaTiO}_3$  shows piezoelectric behaviour, which is referred to as pseudo-piezoelectricity [25]. This behaviour was also investigated by *in-situ* high-energy X-ray diffraction (HEXRD) studies. However, there is a need to understand the origin of pseudo-piezoelectricity in FAST sintered  $\text{CaTiO}_3$  and structural changes which triggered this behaviour.

FAST, which is also often called spark plasma sintering (SPS), is a technique used for the rapid densification of powders by applying pulsed directed current and mechanical load simultaneously to assist the sintering in a protective gas atmosphere or vacuum. The electric current is essential to achieve high densification at lower temperatures with shorter sintering time [26-28]. The advantages of FAST are higher permittivity in ferroelectrics, improved bonding quality and reduced impurity segregation at grain boundaries [24]. Additionally, the sintering atmosphere plays an important role for the stoichiometry, i.e. oxidation number or formation of defects, in the sintered materials [29-31]. The main advantages of FAST are very high heating and cooling rates, which enhance densification over grain growth [24, 32]. Accordingly, it is possible to achieve a high density of grain boundaries with a defective bulk nanostructure which directly influences the physical properties, in particular, the electrical properties of the densified material [24].

Therefore, polycrystalline  $\text{CaTiO}_3$  samples prepared by conventional and FAST sintering have been investigated in detail. Nanostructured  $\text{CaTiO}_3$  was synthesized by sol-gel procedure and densified using conventional and FAST sintering methods. The samples have been examined by HEXRD, scanning electron microscopy (SEM) and X-ray photoelectron spectroscopy (XPS) to investigate their composition, morphology, microstructure and structural defects. Furthermore, direct and inverse piezoelectric behaviour of the samples were investigated. The structural changes after conventional and FAST sintering as well as their piezoelectric behaviour are also studied and compared.

## 2. Materials and methods

### 2.1. Sample preparation

$\text{CaTiO}_3$  was synthesized by sol-gel method. Calcium nitrate tetrahydrate ( $\text{Ca}(\text{NO}_3)_2 \cdot 4\text{H}_2\text{O}$ ) with a purity of 99.0% and titanium isopropoxide ( $\text{Ti}(\text{OC}_3\text{H}_7)_4$ ) with a purity of  $\geq 97.0\%$  were used with equal molar ratios of calcium and titanium as precursors.  $\text{Ca}(\text{NO}_3)_2 \cdot 4\text{H}_2\text{O}$  and  $\text{Ti}(\text{OC}_3\text{H}_7)_4$  were dissolved separately in ethanol using a magnetic stirrer and an ultrasonic bath for 0.5 h. Then, the solution of  $\text{Ca}(\text{NO}_3)_2 \cdot 4\text{H}_2\text{O}$  was added drop-wise in  $\text{Ti}(\text{OC}_3\text{H}_7)_4$  solution and stirred at room temperature for 24 h at 250 rpm. The resulting solution was dried with a spray dryer using an inlet temperature of 190 °C for moisture evaporation and an outlet temperature of 100 °C to control the final moisture content of the powder [33]. Afterwards, the powder was dried in an oven at 180 °C for 2 h to complete moisture evaporation and calcined at 650 °C in air.

The calcined powder was densified using an HP D5 FAST unit from FCT Systeme GmbH Rauenstein, located in the Tycho Sinterlab Rostock, Germany. Graphite dies were filled with calcined  $\text{CaTiO}_3$  powder. Additionally, graphite foil

1 was placed between the powder and inner walls of the die and punched to prevent the powder from reacting with  
2 the die and to ensure a good electric contact. The sintering was performed in a vacuum of approximately 1 mbar.  
3 The applied pressure was 76 MPa and the heating rate was set to 100 K/min.

4 In preliminary experiments, the sintering temperature was varied to ensure good densification of the sample. The  
5 temperature was varied from 1000 °C to 1100 °C. However, as the temperature increases, the carbon diffusion also  
6 increases from the graphite foil to the sample, resulting in a change of colour of CaTiO<sub>3</sub> from white to grey. This also  
7 affects the electrical properties of CaTiO<sub>3</sub>. Motivated by this, a sintering temperature of 1025 °C was selected to  
8 achieve maximum densification and to avoid carbon diffusion.

9 The sintering temperature in the FAST process was held for 5 minutes. Afterwards, the sample was cooled down.  
10 Between 1025 °C to 400 °C the cooling rate was approximately 208 K/min. It is important to mention that due to  
11 technical limitations, the heating process above 400 °C was controlled by an optical pyrometer, and below 400 °C  
12 was monitored by a thermocouple. The optical pyrometer was focused in a hole drilled in the upper part of a  
13 graphite punch, and the thermocouple was attached to the graphite die. The sintered CaTiO<sub>3</sub> was cleaned from the  
14 protective graphite foil using a sandblaster.

15 For comparison, the calcined CaTiO<sub>3</sub> powder was also sintered using conventional sintering. In the beginning, a green  
16 pellet was produced using a press model PW 40 manufactured by P/O/WEBER GmbH. The powder was filled in a  
17 stainless-steel die and uniaxially pressed with approximately 510 MPa for 5 minutes. Then, the green pellet was  
18 removed from the stainless-steel die and placed in an oven model RHTH 120/600/18 manufactured by Nabertherm  
19 GmbH. The sample was heated to a sintering temperature of 1200 °C with a heating rate of 7 K/min. The  
20 temperature was kept constant for 4 h. Afterwards, the sample was cooled down to room temperature.

21 The relative densities ( $\rho_{rel}$ ) of the conventionally and the FAST sintered samples were determined to be  $\rho_{rel} =$   
22  $(83.7 \pm 0.5) \%$  and  $\rho_{rel} = (91.2 \pm 0.4) \%$  using Archimedes method. For further investigations, a cylindrically shaped  
23 specimen with a diameter of 10 mm were precisely cut using a diamond band saw to adjust the height of 2 mm. The  
24 final dimensions of the specimen for further experiments were 10 mm x 2 mm (diameter x height).

25 Sputter coating was used to apply electrodes on both sides of cylindrically shaped samples for piezoelectric  
26 measurements. The sputter coater, model SC7620 manufactured by quorum technologies limited, was equipped  
27 with a silver source, and sputtering was performed in an argon environment. The final thickness of silver electrodes  
28 on the CaTiO<sub>3</sub> samples was approximately 270 nm.

## 29 **2.2. Experimental methods**

30 HEXRD was carried out at the high energy material science beamline P07b located at high brilliance synchrotron  
31 radiation storage ring PETRA III, DESY, Hamburg. The storage ring parameters used were 6 GeV of energy and a  
32 current of 100 mA. A two meter long standard PETRA undulator was the source of X-rays. An indirect water-cooled  
33 single bounce monochromator with a Si(220) Laue crystal was used to select the radiation with a wavelength of

$\lambda=0.1424 \text{ \AA}$  [34, 35]. The experiments were performed in transmission Debye-Scherrer geometry with a sample to detector distance of 1230 mm. The diffraction patterns were collected with a 2D-area PerkinElmer detector.

The morphology of the samples was analysed by a field emission SEM (FE-SEM, MERLIN® VP Compact, Co. Zeiss, Oberkochen). The samples were mounted on SEM-carriers with adhesive conductive carbon tape (co. PLANO, Wetzlar) and coated with carbon under vacuum (EM SCD 500, Co. Leica, Bensheim).

XPS was performed to determine the different binding energies of the calcium and titanium species using a PHI 5600ci spectrometer. The source of X-rays was an Al-cathode and after monochromatization, Al-K $\alpha$  with energy of 1486.7 eV was selected. The measurements were performed in grazing emission geometry with an electron emission angle of 37° with respect to the surface normal. A low-energy electron flood gun was used to deliver the electrons to the sample surface in order to neutralize the surface charge during data acquisition. To obtain detailed spectra, an analyser with 5.85 eV pass energy and 0.05 eV step width was used. Before the measurement, samples were kept in floodgate in vacuum ( $\approx 10^{-7}$  mbar) for approximately two hours. Additionally, the Shirley background was subtracted for all spectra before the fitting procedure, and the data were analysed by assuming Pseudo-Voigt line shape [36].

Measurements to investigate both the direct and inverse piezoelectric effects were carried out. The direct piezoelectric measurements were performed using a dynamic method. The setup was a modification of the one from Fukada and Yasuda [4]. The schematic diagram of the modified setup is presented in Figure 1. An alternating voltage of 10 V generated by a RIGOL DG4062 function generator was applied to the piezo-actuator. Moreover, a frequency of 10 Hz was selected. Consequently, the oscillating force was transmitted to the sample. When a piezoelectric material is used as a sample, an alternating voltage was produced due to the direct

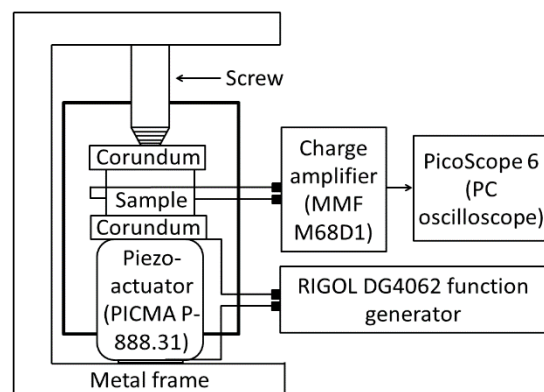


**Figure 1:** Schematic diagram of setup for direct piezoelectric measurements by dynamic method.

piezoelectric effect. This produced alternating voltage was collected using MMF M68D1 charge amplifier. The measurements were recorded with the help of PicoScope 6 (pico technology), which was attached to the charge amplifier. First, glass as a non-piezoelectric material (NPM) with the same dimensions as the sintered samples was clamped inside the metal frame between the screw and the commercial piezo-actuator (type PICMA P-888.31 produced by PI ceramics) to perform the measurement. NPM was used as reference material to determine the maximum noise of the setup. Afterwards, the conventionally and the FAST sintered CaTiO $_3$  were investigated. It is worth mentioning that the samples were isolated from the frame using corundum which was fixed with the screw and the piezo-actuator. All measurements were taken with a gain of 1000 mV/pC of the charge amplifier.

The inverse piezoelectric effect was investigated using FT analyzer 2000 E of aixACCT systems GmbH. The sample holder was connected with FT analyser 2000 E and high voltage trek amplifier to apply a strong electric field to the sample. Triangular voltage excitation signals were used to carry out the measurements. Displacements of samples due to the inverse piezoelectric effect were determined using double beam laser interferometer (aixDBLI) which was

also connected with the sample holder. Data of displacement and current density (J)-electric field characteristic curves were traced by aixPlover software (aixACCT systems GmbH). The values of  $d_{33+}^*$  and  $d_{33-}^*$  were computed by linear regression slope of displacement versus electric field from maximum values of positive and negative electric field to zero electric field (non-switching), respectively.

### 3. Results

#### 3.1. High energy X-ray diffraction

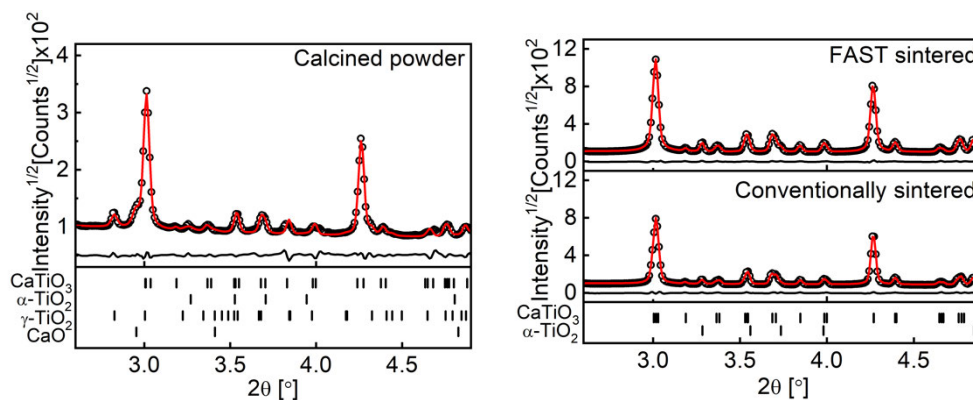


**Figure 2:** HEXRD patterns of the calcined powder (left), the conventionally and the FAST sintered  $\text{CaTiO}_3$  (right). Black dots – experimental pattern and red line – fitted pattern. Below each diffractogram the differential pattern is presented as a black line. Furthermore, corresponding Bragg positions of all contributed phases are shown.

HEXRD patterns were integrated into  $5^\circ$  azimuthal steps and all patterns were processed by Rietveld refinement [37] using the program MAUD [38, 39]. The experimental, fitted, and differential patterns of the calcined  $\text{CaTiO}_3$  powder, the conventionally and the FAST sintered samples are presented in Figure 2 with the Bragg positions of the corresponding phase. In all patterns, orthorhombic (pbm) phase of  $\text{CaTiO}_3$  is present. The crystallite sizes (CS) of the calcined powder, the conventionally and the FAST sintered  $\text{CaTiO}_3$  are presented in Table 1. It is determined that the crystallite size of the FAST sintered  $\text{CaTiO}_3$  increased significantly as compared to calcined powder, due to the recrystallization process during sintering [24]. The conventionally sintered sample showed even larger crystallite size, as a result of the longer sintering time. It is also possible that small fraction of amorphous phase was present in the calcined powder which was crystalline during sintering. Small amounts of other phases, such as brookite ( $\gamma\text{-TiO}_2$ ), rutile ( $\alpha\text{-TiO}_2$ ) and calcium oxide (CaO), were found in the calcined powder. However, after conventional and also after FAST sintering, only  $\alpha\text{-TiO}_2$  phase was present in the samples. This indicates that  $\text{TiO}_2$  and CaO form  $\text{CaTiO}_3$  phase upon the sintering process. It is also possible that excessive amounts of  $\gamma\text{-TiO}_2$  transformed into  $\alpha\text{-TiO}_2$ , which is more stable than  $\gamma\text{-TiO}_2$ .  $\gamma\text{-TiO}_2$  transforms to  $\alpha\text{-TiO}_2$  when heated [40]. The weight fractions of the corresponding phases, as well as  $R_w$  and  $R_b$  values from the Rietveld refinement, are also presented in Table 1.

CaTiO <sub>3</sub>	CS [nm]	Phases [wt%]				R <sub>w</sub> [%]	R <sub>b</sub> [%]
		CaTiO <sub>3</sub>	α-TiO <sub>2</sub>	γ-TiO <sub>2</sub>	CaO		
<b>Calcined powder</b>	98±3	83.8±0.5	4.2±0.3	6.7±0.4	5.4±0.6	6.77	4.61
<b>Conventionally sintered</b>	406±4	94.6±0.3	5.4±0.1	-	-	6.46	4.24
<b>FAST sintered</b>	200±1	94.4±0.2	5.6±0.6	-	-	5.08	3.32

**Table 1:** Determined crystallite sizes (CS) of the calcined powder, the conventionally and the FAST sintered CaTiO<sub>3</sub>, weight fractions (wt%) of contributing phases, and R<sub>w</sub> and R<sub>b</sub> values from Rietveld refinement are given.

### 3.2. Scanning electron microscopy

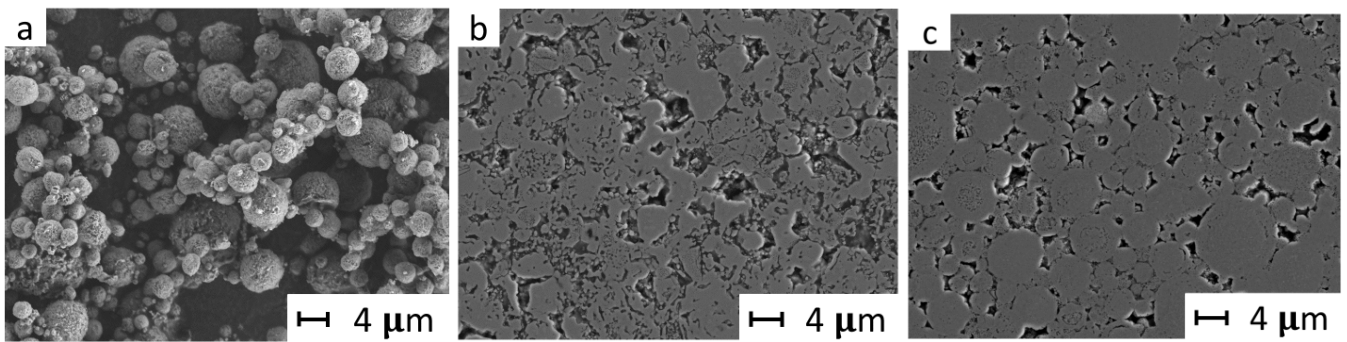


**Figure 3:** Exemplary SEM images of (a) the calcined powder, (b) the conventionally and (c) the FAST sintered CaTiO<sub>3</sub>.

Figures 3a, b and c show the exemplary SEM images of the calcined powder, the polished surfaces of the conventionally and the FAST sintered CaTiO<sub>3</sub>, respectively. The particle size of the powder and grain sizes of sintered samples were determined using ImageJ software [41], and the average particle and grain sizes were estimated assuming a log-normal distribution (see supplementary). It can be seen in Figure 3a that most of the particles having the average particle size of  $(2.3 \pm 0.1) \mu\text{m}$  are spherical in shape and significantly larger than the determined crystallite size. The grain shapes of the FAST sintered sample are spherical having the average grain size of  $(2.5 \pm 0.1) \mu\text{m}$  but the one of conventionally sintered sample  $(7.2 \pm 0.3) \mu\text{m}$  have ambiguous shape, probably due to abnormal Ostwald ripening which also causes irregular elongation of grains [24]. Additionally, the pores can be observed in the SEM images as dark areas between the brighter grains. These pores may be beneficial for osteogenesis.

### 3.3. X-ray photoelectron spectroscopy

High-resolution measurements of Ti-2p, Ca-2p and O-1s peaks of the calcined powder, the conventionally sintered and the FAST sintered samples were investigated using XPS. Figures 4a and 4b present the fitted spectra of Ti-2p<sub>3/2</sub> and Ca-2p<sub>3/2</sub> species in FAST sintered CaTiO<sub>3</sub>, respectively. The spectra of Ti-2p<sub>3/2</sub> in Figure 4a is plotted in the square root scale to achieve the same statistical derivation on the maxima and the background compared to Ca-2p<sub>3/2</sub> in Figure 4b [42].

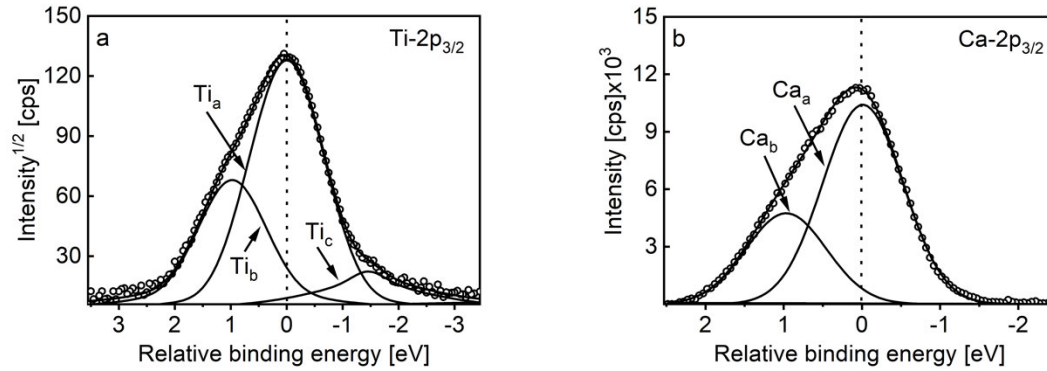


**Figure 4:** High-resolution spectra of (a)  $Ti-2p_{3/2}$  and (b)  $Ca-2p_{3/2}$  peaks of the FAST sintered  $CaTiO_3$  after background subtraction. Experimental (black dots) and fitted curves (black line) with corresponding species are presented.

Three types of titanium species, i.e.  $Ti_a$ ,  $Ti_b$  and  $Ti_c$ , can be seen in Figure 4a.  $Ti_a$  specie corresponds to the normal structure of  $TiO_6$  octahedral. Whereas,  $Ti_b$  and  $Ti_c$  are newly formed species detected in bulk  $CaTiO_3$  after FAST sintering. In Figure 4b, two different types of calcium species, i.e.  $Ca_a$  and  $Ca_b$ , can also be identified. Additionally, it was also observed that the spectral peaks of  $Ti-2p_{3/2}$  and  $Ca-2p_{3/2}$  and  $O-1s$  of FAST sintered  $CaTiO_3$  are broadened compared to the spectral peaks of the calcined powder and the conventionally sintered  $CaTiO_3$  (see supplementary). This fact indicates different chemical environments in the FAST sintered sample, which is a result of the FAST sintering process [43, 44], and discussed in section 4.3. The full width half maximum (fwhm) and quantities of particular species are presented in the supplementary.

### 3.4. Piezoelectric measurements

Both direct and inverse piezoelectric measurements were carried out for the conventionally and the FAST sintered  $CaTiO_3$  samples. The results of the direct piezoelectric measurements are presented in Figure 5. The shown alternating input voltage (black line) is the voltage applied to the piezo-actuator for its oscillation. It can be seen that a small alternating output voltage (green line) is produced by NPM ( $V_{NPM}$ ) without electrodes. This is interpreted as the maximum noise produced by the setup. The signal ( $V_{CaTiO_3}$ ) of the conventionally sintered  $CaTiO_3$  (blue line) is very close to the maximal noise of the setup. However, the alternating output voltage ( $V_{CaTiO_3}$ ) of the FAST sintered  $CaTiO_3$  (red line) [25], is significantly larger than the ones of the other tested samples. This significant increase in  $V_{CaTiO_3}$  is the first evidence that FAST sintered  $CaTiO_3$  showing piezoelectric behaviour. The charge (Q) produced through the direct piezoelectric effect is calculated by Equation 1 and presented in Table 2:

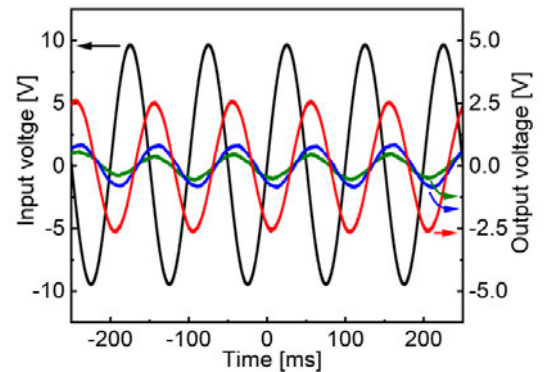


**Figure 5:** Time dependent voltage measurement of the NPM (green line), the conventionally (blue line) and the FAST sintered (red line)  $CaTiO_3$  measured with the direct piezoelectric effect. Additionally, the input voltage of the piezo-actuator is presented (black line).

$$Q_{CaTiO_3} = \frac{V_{CaTiO_3}}{Gain} - \frac{V_{NPM}}{Gain} \quad (1)$$

1 Measurements to investigate the inverse piezoelectric effect of the  
 2 conventionally and the FAST sintered  $\text{CaTiO}_3$  are presented in Figure 6.  
 3 It can be seen that no measurable displacement occurred in 1<sup>st</sup> and 2<sup>nd</sup>  
 4 cycles of conventionally sintered  $\text{CaTiO}_3$ . Moreover, there is no flow of  
 5 electric current in both cycles. However, in the FAST sintered  $\text{CaTiO}_3$ , a  
 6 butterfly-shaped hysteresis curve can be seen. During the 1<sup>st</sup> cycle of  
 7 electric field [25], the displacement is observed, when the electric field  
 8 was increased from 0 kV/cm to +10 kV/cm. This displacement then  
 9 decreases, when electric field goes from +10 kV/cm to 0 kV/cm. The  
 10 same kind of displacement is also observed on the negative side of the  
 11 electric field. Finally, it goes approximately back to its initial position  
 12 when the electric field is again reduced to 0 kV/cm. This observation is  
 13 the second evidence of piezoelectricity in FAST sintered  $\text{CaTiO}_3$ . The  
 14 same process is repeated during the 2<sup>nd</sup> cycle, and the displacement is  
 15 observed again, but this time the conductivity increases slightly in the  
 16 direction of the positive electric field as compared to the 1<sup>st</sup> cycle. In  
 17 addition, there is an overflow of electric current in the negative  
 18 electric field direction which was beyond the limitations of the  
 19 experimental setup. The constant displacement of sample during the  
 20 overflow of electric current can also be seen. This behaviour is  
 21 observed because the current reached the maximum driving current.  
 22 As a result, the amplifier reduced the voltage and kept it on a constant  
 23 level (see supplementary). This constant voltage also kept constant the displacement generated by the sample.  
 24 However, current goes back to a measurable value when the electric field is reduced to approximately -2 kV/cm and  
 25 then returns to 0 kV/cm. Similarly, normal displacement behaviour can also be seen again. The values of  $d_{33+}^*$  and  
 26  $d_{33-}^*$  computed by Figure 6 are presented in Table 2. In this work, only  $d_{33+}^*$  value for the 2<sup>nd</sup> cycle of FAST sintered  
 27  $\text{CaTiO}_3$  is reported, because of the overflow in negative electric field direction.

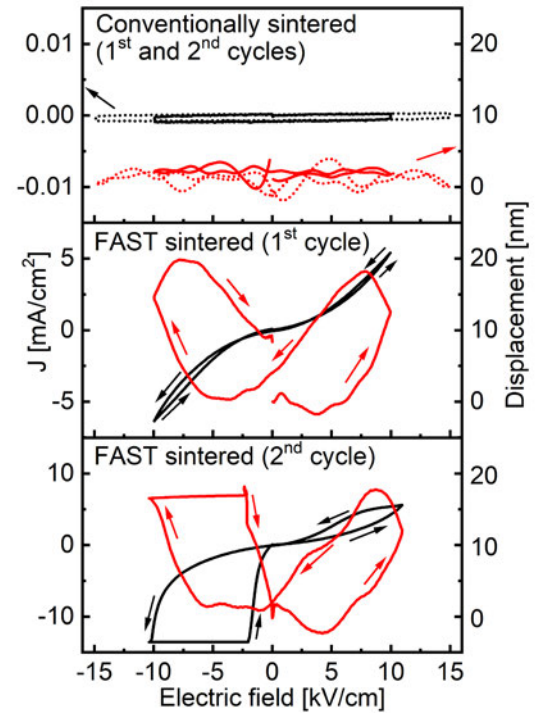


**Figure 6:** Displacement (red colour) and  $J$ -electric field (black colour) characteristic curves with a maximal electric field of  $\pm 10$  kV/cm (1<sup>st</sup> cycle – line) and  $\pm 15$  kV/cm (2<sup>nd</sup> cycle – dots) applied to the conventionally sintered as well as (1<sup>st</sup> cycle) maximal  $\pm 10$  kV/cm and (2<sup>nd</sup> cycle) maximal  $\pm 11$  kV/cm to the FAST sintered  $\text{CaTiO}_3$ , determined at room temperature and with a frequency of 1 Hz.

28 It is worth mentioning that  $\text{CaTiO}_3$  is known as electrostrictive material, but the observed effects are strong evidence  
 29 for the piezoelectric behaviour generated in FAST sintered  $\text{CaTiO}_3$ . In electrostrictive materials, no direct  
 30 piezoelectric effect can be observed because a mechanical deformation does not produce surface charges.  
 31 Moreover, the reverse of the electric field does not reverse the direction of deformation, meaning that no hysteresis  
 32 curve can be observed in electrostrictive materials. However, the typical butterfly displacement curve due to the  
 33 inverse piezoelectric effect is detectable for the FAST sintered nanostructured  $\text{CaTiO}_3$ .

CaTiO <sub>3</sub>	Q [pC]
Piezoelectric constants [pm/V]	
1 <sup>st</sup> cycle	$d_{33+}^* \sim 7.13 \pm 0.4$ $d_{33-}^* \sim -5.95 \pm 0.3$
2 <sup>nd</sup> cycle	$d_{33+}^* \sim 7.19 \pm 0.3$

**Table 2:** The determined charge of the FAST sintered CaTiO<sub>3</sub> and the piezoelectric constant values are given.

## 4. Discussion

### 4.1. Lattice parameters

Lattice distortions in any material result in the change of lattice parameters [45]. Therefore, lattice parameters of the CaTiO<sub>3</sub> orthorhombic phases of the calcined powder, the conventionally and the FAST sintered CaTiO<sub>3</sub> are compared and presented along with literature values (dotted lines) [46] in Figure 7. In the calcined powder, the lattice parameter *b* is very close to the corresponding literature value, but *a* and *c* are significantly larger. This may be caused by defects being present on well-defined lattice sites [47]. A significant decrease in the lattice parameters *a* and *c* is noticed, while *b* remains approximately constant for the conventional sintered sample. This decrease in lattice parameters can be interpreted as the

removal of oxygen vacancies from lattice sites [48] (in the absence of oxygen atom, Ti-Ti atoms can repel each other due to Coulomb effect which can cause the increase in lattice parameters). For example, if oxygen vacancies were present in the calcined powder, they could cure themselves during conventional sintering in air. As a result, the lattice parameters of conventionally sintered CaTiO<sub>3</sub> are comparable to literature values. For the FAST sintered sample, the lattice parameters *b* and *c* decrease slightly, and *a* remains approximately constant compared to the calcined powder. The lattice parameters *a* and *c* are still significantly larger than the literature values, but *b* decreases significantly. The lattice parameters differ from literature values probably caused by a large amount of oxygen lattice vacancies and distortions produced by defects inside the lattice. These defects can be produced during the FAST sintering process in reducing atmosphere and in the presence of graphite, similar to those observed in BaTiO<sub>3</sub> under reducing sintering conditions [31].

### 4.2. Lattice strain

Apart from the integration of complete Debye-Scherrer rings, HEXRD patterns were also partially integrated every 85° azimuthal steps with a step width of 5°. These individual azimuthal sectors 0° (180°) and 90° (270°) are parallel and perpendicular to the sintering field (SF), respectively, which was applied during FAST sintering process by the direct current pulses (see supplementary).

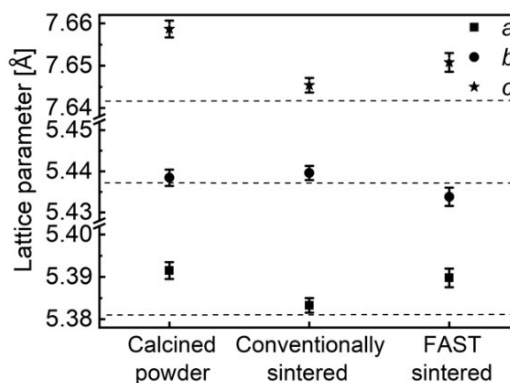


**Figure 7:** Lattice parameters of the calcined powder, the conventionally and the FAST sintered CaTiO<sub>3</sub>. The literature values of lattice parameters are also presented as dotted lines.

The lattice parameters of the individual azimuthal sector, i.e. 0°, 90°, 180° and 270°, were extracted by Rietveld refinement [37], and then the strain ( $\varepsilon$ ) was calculated by using Equation 2:

$$\varepsilon = \frac{q - q_0}{q_0} \quad (2)$$

where  $q$  denotes the value of lattice parameters of the azimuthal sector when taking it as a starting point, i.e. 0°, 90°, 180° and 270°, and  $q_0$  is the value of lattice parameters of the azimuthal sector when taking it as an ending point, i.e. 90°, 180°, 270° and 0°.

The lattice strain in lattice parameters  $a$ ,  $b$  and  $c$  as a function of initial to final azimuthal sectors is presented in Figure 8. It can be seen that no significant lattice strain (blue colour) is present in lattice parameters  $a$ ,  $b$  and  $c$  in the conventionally sintered sample. In the FAST sintered sample, maximum lattice strain (red colour) is present in the lattice parameter  $c$ . Furthermore, lattice strain for  $a$  and  $b$  is also observed. This suggests that the maximum lattice strain induced by FAST sintering is in  $c$  direction. In  $a$  and  $b$  direction, the strain is induced by a lattice redistribution, which is originated by the distortion produced by  $c$ . It is also worth mentioning that if lattice strain in  $a$  and  $c$  is positive, then in  $b$  it is negative, and if lattice strain in  $a$  and  $c$  is negative, then it is positive in  $b$ . This means that the Debye-Scherrer rings of FAST sintered  $\text{CaTiO}_3$  are not circular but elliptical in shape due to structural distortions which ultimately generated electric dipole moments by the shifting of negative and positive charges [25].

### 4.3. Lattice point defects

Lattice distortions can have significantly different binding energies compared to non-distorted structures, and therefore, these can be detected by XPS [49].  $\text{Ti}_a$  specie, shown in Figure 4a, corresponds to the non-distorted (normal) structure of  $\text{TiO}_6$  octahedral. Whereas, it is suggested that newly formed  $\text{Ti}_b$  specie can be related to a distorted structure of the  $\text{TiO}_6$  octahedra [50]. Additionally, a small amount of reduced  $\text{Ti}_c$  specie located in the low energy shoulder of the  $\text{Ti}-2p_{3/2}$  is likely to be caused by oxygen vacancies produced by FAST sintering in reducing atmosphere [24]. This reducing atmosphere can be a reason to a shift of binding energy of  $\text{Ti}-2p_{3/2}$  indicating the presence of  $\text{TiO}_5$  octahedra, due to the reduction of  $\text{Ti}^{4+}$  specie to  $\text{Ti}^{3+}$  [22]. A broadening in the fwhm of O-1s spectrum of FAST sintered sample is another indication of the formation of oxygen vacancy which is larger compared to the calcined powder or the conventionally sintered sample (see supplementary). This reduction of normal  $\text{TiO}_6$  octahedra can be associated with the generation of electric dipoles. Moreover, it is likely that  $\text{Ca}_a$  specie in Figure 4b is attributed to  $\text{Ti}_a$  specie, referring to domains with non-distorted unit cells, and  $\text{Ca}_b$  is attributed to  $\text{Ti}_b$ , referring to domains with distorted unit cells. This shows that there are two different chemical environments present in the FAST

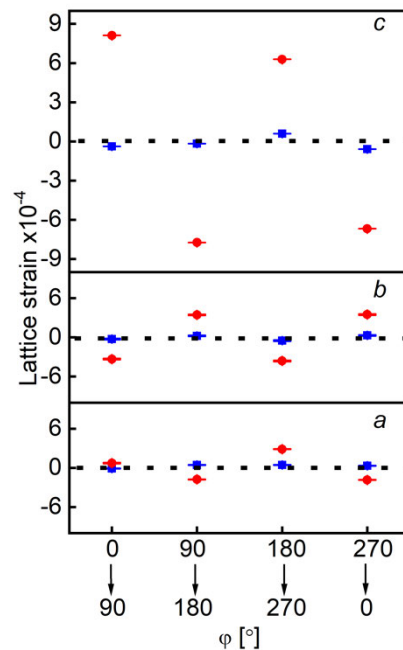


**Figure 8:** Lattice strain in lattice parameters  $a$ ,  $b$  and  $c$  of the conventionally (blue colour) and the FAST sintered (red colour)  $\text{CaTiO}_3$  vs azimuthal sector.

1 sintered  $\text{CaTiO}_3$ . These two types of chemical environments could be interpreted as one originated by stress  
 2 (distorted structure) and another one without induced stress (non-distorted structure).

### 3 4.4. Structural defects in FAST sintered $\text{CaTiO}_3$

4 The 3D graphical representation of  $\text{CaTiO}_3$  unit cell is presented in Figure 9 to visualize its defective structure. There  
 5 are two defect sites which can be present in the octahedron, i.e. top-to-top (O1) or in-plane (O2). Oxygen is an anion  
 6 which attracts Ti cation. If an oxygen vacancy is formed, the repulsion between Ti-Ti atoms is created due to identical  
 7 charges. This means that it can change the charge configuration similar to  $\text{SrTiO}_3$  [51]. This is interpreted as the  
 8 elongation of lattice parameter  $c$  (due to repulsion between Ti-Ti atoms) causing slight straightening of bond angles.  
 9 This straightening of bond angles was analysed by using the VESTA program [52]. The Rietveld refined parameters at  
 10  $0^\circ$  azimuthal sector (parallel to SF) and  $90^\circ$  azimuthal sector (perpendicular to SF) were extracted. This data, i.e.  
 11 individual unit cell model, was then visualized, and bond lengths and bond angles were compared.

12 It was noticed that average bond angle O1-O1-  
 13 O1 connected in-between Ti atoms at  $0^\circ$   
 14 azimuthal sector is slightly decreased relative  
 15 to  $90^\circ$  azimuthal sector (see supplementary),  
 16 which also influenced the bond lengths  
 17 between atoms. It is possible that while  
 18 current flew inside the material due to  
 19 sintering current pulses, electrons might have  
 20 been trapped at sites of oxygen vacancies in  
 21 parallel SF direction. This trapping of electrons  
 22 can cause the compression of lattice parameter  
 23  $c$ . It can be interpreted that O1, O2 and Ti  
 24 atoms are displaced mainly along with the  
 25 lattice parameter  $c$  by forming unequal bond  
 26 distances which also affects the lattice

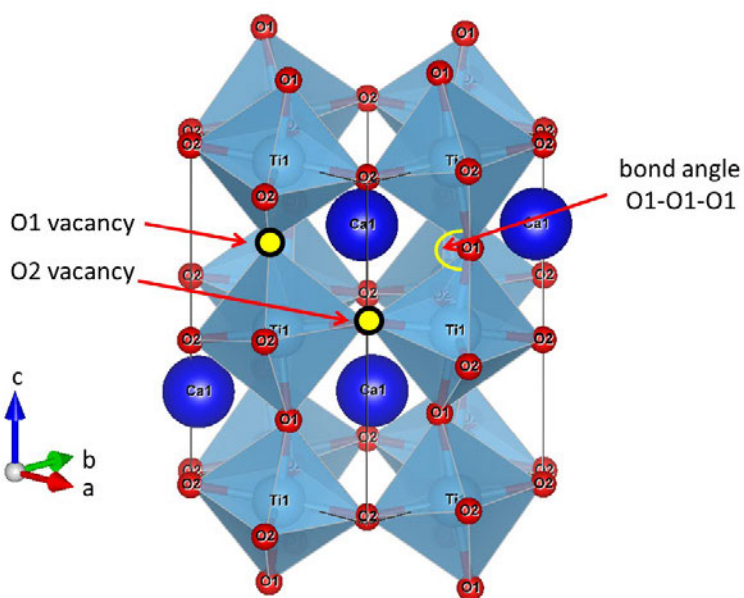


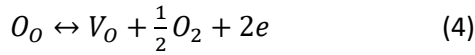
**Figure 9:** 3D Graphical representation of  $\text{CaTiO}_3$  unit cell. Two oxygen vacancies cite (yellow circles) and bond angle O1-O1-O1 are also presented.

27 parameters  $a$  and  $b$ . This unequal distance of bonds generates electric dipole moments by the displacements of  
 28 cations and anions from their equilibrium positions [18]. Whereas, the average bond angle O1-O1-O1 of the  
 29 conventionally sintered sample remained same in both ( $0^\circ$  and  $90^\circ$ ) azimuthal sectors (see supplementary).  
 30 Moreover, these angles are slightly greater as compare to the FAST sintered sample, indicating no elongation of  
 31 lattice parameter  $c$  because of non-straightening of bond angles.

### 32 4.5. Pseudo-piezoelectricity in FAST sintered $\text{CaTiO}_3$

33 As presented in Section 3.4, FAST sintered  $\text{CaTiO}_3$  shows a response for both the direct and inverse piezoelectric  
 34 effect. This observation is referred as a pseudo-piezoelectric effect [25], due to the fact that the space group  $\text{CaTiO}_3$

belongs to is centro-symmetric and does not show piezoelectric behaviour. The observed piezoelectric effect is most likely a result of the defective structure of CaTiO<sub>3</sub>. Oxygen vacancies generate lattice distortions in CaTiO<sub>3</sub> at elevated temperature during the FAST sintering. This process can be described by the following equilibrium [53], using the Kröger-Vink notation [54]:



Here  $O_o$  is lattice oxygen,  $V_o$  is a lattice oxygen vacancy and  $e$  is an electron.

The experimental results suggest the presence of defects due to oxygen vacancies as well as lattice distortion in FAST sintered CaTiO<sub>3</sub>. In general, the defects can be distinguished into lattice point defects such as Ti<sup>3+</sup> states or oxygen vacancies, line defects such as grain boundaries or crystallographic shear planes [55]. The oxygen vacancy, for example, can be at the surface or in the bulk area [56, 57]. The unit cells which connect these areas include the bridging oxygen which is a well defined oxygen position on the border of a domain [58, 59]. It is possible that these defects create local instability of the normal TiO<sub>6</sub> octahedra, which results in a slight shift of the geometrical midpoint. Since the observed Debye-Scherrer rings are elliptical, which is likely due to the distortions in the crystal structure of FAST sintered CaTiO<sub>3</sub>. It means that there is a shift of the charges and therefore electric dipoles are created [25]. If local electric dipoles are present so are local domains. These domains are only present where the distortions are, in other words where the shift of the charges occurred due to strain influenced by oxygen vacancies or/and reduction of Ti<sup>4+</sup> to Ti<sup>3+</sup>. This type of geometrical configurations can lead to piezoelectric behaviour [23, 60]. Presuming that local domains are present due to localized defects, there are two possibilities that might have fulfilled this condition. The first possibility is by suppressing the grain growth and increasing grain boundary areas as pinning points. These grain boundaries can act like blocking positions for migration and prevent diffusion of defects causing permanent electric dipoles [61-63]. The second possibility is preventing the migration of defects into their equilibrium configuration through significantly increasing mobility of domain walls [23]. This can be achieved by rapid cooling from elevated temperature, which freezes the distribution of the defects. Both requirements were probably accomplished by the FAST sintering process. It has an advantage of short heating and cooling times, while applying a pressure, which allows fast densification, limited grain growth and increased grain boundary areas as well as the freezing of the distribution of defects [32, 64]. It has been shown that oxygen vacancies of CaTiO<sub>3</sub> prefer to reside within twin boundary walls being energetically favourable, which results pinning of the walls [58]. Furthermore, oxygen vacancies can preferably exist near grain boundaries as in SrTiO<sub>3</sub> [65].

Another reason for lattice distortions in the investigated sample can be the flow of direct current pulses inside the sample during FAST sintering. Since powder inside the die is not completely homogenous or dense. This feature of the powder creates a complicated network of current. The fluctuating hot spots formed in the path of current due to Joule heating may lead to lattice distortions, which freeze themselves due to rapid heating and cooling rates [24]. Therefore, the observed pseudo-piezoelectricity of FAST sintered CaTiO<sub>3</sub> is most likely a direct result of lattice distortions originated by the formation of localized defects during the sintering process.

1 It is also worth mentioning that the FAST sintered  $\text{CaTiO}_3$  showed a piezoelectric response using the direct  
 2 piezoelectric method without a poling treatment. The reason is likely that some of the electric dipoles already  
 3 aligned themselves during the FAST sintering process due to the huge pulsed direct current. However, the  
 4 conventionally sintered sample did not exhibit a piezoelectric effect even after poling treatment.

5 The displacement observed using the inverse piezoelectric method occurred due to the polarization. It leads to an  
 6 alignment of more electric dipoles (domains switching) by applying a strong electric field. When an electric field is  
 7 applied, electrons (due to trapping) can reduce the metal cations, i.e.  $\text{Ti}^{+4}$  to  $\text{Ti}^{+3}$ . This effect is observed in the J-  
 8 electric field characteristic curve during the 2<sup>nd</sup> cycle (see Figure 6), which shows relatively high conductivity in the  
 9 range of +11 kV/cm to 0 kV/cm as compared to 0 kV/cm to +11 kV/cm. This reveals the change in the concentration  
 10 of defects, because more electrons come from the external source (closed electrical circuit) which influence the flow  
 11 of electrons in an electric field [22]. As a result, it also influences the strength of electric dipoles due to non-  
 12 equilibrium domains with trapped charges and the alignment of electric dipole moments due to the electric field  
 13 [23]. The alignment of electric dipoles becomes stronger in every cycle as more defects are produced. Eventually, the  
 14 material has enough defects and electric dipole density that it opens conducting channels causing an overflow as for  
 15 example in  $\text{SrTiO}_3$  [66]. It is also important to mention that electrical conductivity is a defect sensitive property as  
 16 defects are electrically charged [53]. At a certain limit, defects' concentration can overcome the enthalpy of the  
 17 motion for charge carriers, leading to their diffusion in strong electric field. Therefore, there should be enough  
 18 defects to create electric dipoles with significant strength, but not too many defects to open conducting channels  
 19 causing overflow. This overflow is observed during the 2<sup>nd</sup> cycle in Figure 6 in the negative electric field direction,  
 20 which indicates the disappearance of the pseudo-piezoelectric behaviour.

21 In addition, HEXRD results showed the  $\alpha\text{-TiO}_2$  phase impurity of  $(5.6\pm 0.6)$  wt%, which could also contribute to an  
 22 increasing conductivity, as  $\text{TiO}_2$  can significantly reduce resistivity even in low electric field [22]. Nevertheless, the  
 23 presence of restoring force upon reducing the electric field in every cycle can be seen, which could arise from the  
 24 contribution of stress-induced instability of the ferroelastic domain wall switching. It is also important to mention  
 25 that previously *in-situ* HEXRD investigations showed that the structural changes occurred only in  $\text{CaTiO}_3$  but not in  $\alpha\text{-}$   
 26  $\text{TiO}_2$  phase [25]. Hence, the observed pseudo-piezoelectric behaviour is purely generated by  $\text{CaTiO}_3$ .

#### 27 **4.6. Piezoelectric constant**

28 A complete set of  $d_{ij}$  can be represented by a matrix [67]. This matrix can be deduced based on non-centro-  
 29 symmetric point groups of the crystal. The orthorhombic crystal structure of  $\text{CaTiO}_3$  belongs to centro-symmetric  
 30 point group (mmm). This implies that all of its  $d_{ij}$  values are zero. However, in the defective nanostructure of FAST  
 31 sintered  $\text{CaTiO}_3$ , the  $d_{33+}$  and  $d_{33-}$  (Table 2) values are not zero. These values are relatively small as compare to  
 32 well-known perovskite piezoelectric ceramics. The reason for having small  $d_{33+}$  and  $d_{33-}$  values could be due to low  
 33 electric dipole density and stability. FAST sintered  $\text{CaTiO}_3$  is possibly showing pseudo-piezoelectric behaviour due to  
 34 localized defects with lattice distortions, but not from its normal crystal structure like other perovskite piezoelectric  
 35 ceramics, e.g. PZT,  $\text{BaTiO}_3$  or  $\text{SrTiO}_3$ . Using FAST sintered or similar  $\text{CaTiO}_3$  ceramics as an implant material could be

1 advantageous over commonly used materials due to the pseudo-piezoelectric behaviour, which may increase  
2 osseointegration.

### 3 **5. Conclusions**

4 CaTiO<sub>3</sub> powder was successfully prepared by sol-gel synthesis and densified using FAST and conventional sintering.  
5 The sintered samples are a characteristic of nanostructured orthorhombic (pbnm) CaTiO<sub>3</sub> phase containing a small  
6 amount of  $\alpha$ -TiO<sub>2</sub>. The data confirms that defects like oxygen vacancies as well as lattice strain and distortions are  
7 present in FAST sintered CaTiO<sub>3</sub> which are not observed in the conventionally sintered sample. These defects and  
8 lattice distortions are mainly produced during the FAST sintering process in a reduced atmosphere. The rapid heating  
9 and cooling rates in FAST sintering freeze the distorted state of the sample. Moreover, the FAST sintered CaTiO<sub>3</sub> has  
10 smaller grain sizes compared to the conventionally sintered CaTiO<sub>3</sub> resulting in a larger amount of grain boundary  
11 areas. These grain boundary areas can act as pinning points, as well as blocking positions for migrations and diffusion  
12 of defects until a strong electric field is applied repeatedly. The defects in the FAST sintered CaTiO<sub>3</sub> are highly  
13 localized and lead to permanent electric dipoles. Hence, a pseudo-piezoelectric response is generated only in the  
14 FAST sintered sample, since it is generated by a distorted structure. The effect was measured by both the direct and  
15 inverse piezoelectric methods. The charge produced on the FAST sintered sample is  $(2.1\pm 0.3)$  pC and typical  
16 displacement hysteresis curve is also detected. However, no charge is produced in the conventionally sintered  
17 sample, and displacement hysteresis curve is also not observed. These observations confirmed that pseudo-  
18 piezoelectric behaviour is triggered by FAST sintering due to defective structure and not by conventional sintering.  
19 These findings are promising for CaTiO<sub>3</sub> to be used as a bone implant material to facilitate cell-materials interaction  
20 and improve osseointegration.

### 21 **Acknowledgements**

22 This work was financially supported by the DFG Graduate School *welisa* (project no. 1506). The assistance of Dr.  
23 Richard Dietrich in sputter coating and Carola Ladewig for polishing of samples is acknowledged. Rico Schnierer is  
24 also appreciated for useful discussion.

### 25 **Appendix. Supplementary data**

26 Supplementary data associated with this article can be found in the online version (link).

## 1 Bibliography

- [1] F. Zhang and E. Burkel, "Novel titanium manganese alloys and their macroporous foams for biomedical applications prepared by field assisted sintering," in *Biomedical Engineering, Trends in Materials Science: InTech*, 2011.
- [2] F. Zhang, Y. Quan, M. Reich, O. Kessler, and E. Burkel, "Sintering and heat treatment of titanium alloys by pulsed electric current sintering," in *Sintering Applications: InTech*, 2013.
- [3] S. Spriano et al., "Bioactive titanium surfaces," 2010.
- [4] E. Fukada and I. Yasuda, "On the piezoelectric effect of bone," *Journal of the physical society of Japan*, vol. 12, no. 10, pp. 1158-1162, 1957.
- [5] S. Singh and S. Saha, "Electrical properties of bone. A review," *Clinical orthopaedics and related research*, no. 186, pp. 249-271, 1984.
- [6] D. Wieland, C. Krywka, E. Mick, R. Willumeit-Römer, R. Bader, and D. Klues, "Investigation of the inverse piezoelectric effect of trabecular bone on a micrometer length scale using synchrotron radiation," *Acta biomaterialia*, vol. 25, pp. 339-346, 2015.
- [7] A. Rutkovskiy, K.-O. Stenslökken, and I. J. Vaage, "Osteoblast differentiation at a glance," *Medical science monitor basic research*, vol. 22, p. 95, 2016.
- [8] A. H. Rajabi, M. Jaffe, and T. L. Arinze, "Piezoelectric materials for tissue regeneration: A review," *Acta biomaterialia*, vol. 24, pp. 12-23, 2015.
- [9] Q. Wang et al., "Manufacture and Cytotoxicity of a Lead-free Piezoelectric Ceramic as a Bone Substitute—Consolidation of Porous Lithium Sodium Potassium Niobate by Cold Isostatic Pressing," *International journal of oral science*, vol. 1, no. 2, pp. 99-104, 2009.
- [10] F. R. Baxter, C. R. Bowen, I. G. Turner, and A. C. Dent, "Electrically active bioceramics: a review of interfacial responses," *Annals of biomedical engineering*, vol. 38, no. 6, pp. 2079-2092, 2010.
- [11] R. Tazaki, D. Fu, M. Itoh, M. Daimon, and S.-y. Koshihara, "Lattice distortion under an electric field in BaTiO<sub>3</sub> piezoelectric single crystal," *Journal of Physics: Condensed Matter*, vol. 21, no. 21, p. 215903, 2009.
- [12] W. Chen, H. L. Chan, F. Yiu, K. Ng, and P. Liu, "Water-induced degradation in lead zirconate titanate piezoelectric ceramics," *Applied physics letters*, vol. 80, no. 19, pp. 3587-3589, 2002.
- [13] N. Ohtsu, K. Sato, K. Saito, K. Asami, and T. Hanawa, "Calcium phosphates formation on CaTiO<sub>3</sub> coated titanium," *Journal of Materials Science: Materials in Medicine*, vol. 18, no. 6, pp. 1009-1016, 2007.
- [14] K. Hamada, M. Kon, T. Hanawa, K. i. Yokoyama, Y. Miyamoto, and K. Asaoka, "Hydrothermal modification of titanium surface in calcium solutions," *Biomaterials*, vol. 23, no. 10, pp. 2265-2272, 2002.
- [15] T. J. Webster, C. Ergun, R. H. Doremus, and W. A. Lanford, "Increased osteoblast adhesion on titanium-coated hydroxylapatite that forms CaTiO<sub>3</sub>," *Journal of Biomedical Materials Research Part A: An Official Journal of The Society for Biomaterials, The Japanese Society for Biomaterials, and The Australian Society for Biomaterials and the Korean Society for Biomaterials*, vol. 67, no. 3, pp. 975-980, 2003.
- [16] A. Kholkin, N. Pertsev, and A. Goltsev, "Piezoelectricity and crystal symmetry," in *Piezoelectric and Acoustic Materials for Transducer Applications: Springer*, 2008, pp. 17-38.
- [17] J. W. Anthony, R. A. Bideaux, K. W. Bladh, and M. C. Nichols, "Handbook of mineralogy, Volume IV, arsenates, phosphates, vanadates," 1-680, Mineralogical Society of America, Chantilly, Virginia, 2000.
- [18] A. Yoshiasa, T. Nakatani, A. Nakatsuka, M. Okube, K. Sugiyama, and T. Mashimo, "High-temperature single-crystal X-ray diffraction study of tetragonal and cubic perovskite-type PbTiO<sub>3</sub> phases," *Acta crystallographica Section B, Structural science, crystal engineering and materials*, vol. 72, no. Pt 3, pp. 381-8, Jun 1 2016, doi: 10.1107/S2052520616005114.
- [19] A. Erba, K. E. El-Kelany, M. Ferrero, I. Baraille, and M. Rérat, "Piezoelectricity of SrTiO<sub>3</sub>: Anab initiodescription," *Physical Review B*, vol. 88, no. 3, 2013, doi: 10.1103/PhysRevB.88.035102.
- [20] T. Nishigaki and S. Hontsu, "Effect of Poling Treatment on Piezoelectric Constant of Pulsed Laser Deposited Hydroxyapatite Thin Films," *Key Engineering Materials*, vol. 631, 2014.
- [21] S. Van Aert, S. Turner, R. Delville, D. Schryvers, G. Van Tendeloo, and E. K. Salje, "Direct observation of ferroelectricity at ferroelastic domain boundaries in CaTiO<sub>3</sub> by electron microscopy," *Adv Mater*, vol. 24, no. 4, pp. 523-7, Jan 24 2012, doi: 10.1002/adma.201103717.
- [22] M. Hantusch, V. Bessergenev, M. C. Mateus, M. Knupfer, and E. Burkel, "Electronic properties of photocatalytic improved Degussa P25 titanium dioxide powder," *Catalysis Today*, vol. 307, pp. 111-118, 2018, doi: 10.1016/j.cattod.2017.11.005.
- [23] T. Rojac, M. Kosec, B. Budic, N. Setter, and D. Damjanovic, "Strong ferroelectric domain-wall pinning in BiFeO<sub>3</sub> ceramics," *Journal of Applied Physics*, vol. 108, no. 7, p. 074107, 2010, doi: 10.1063/1.3490249.
- [24] O. Guillon et al., "Field-assisted sintering technology/spark plasma sintering: mechanisms, materials, and technology developments," *Advanced Engineering Materials*, vol. 16, no. 7, pp. 830-849, 2014.
- [25] A. Riaz, K. Witte, W. Bodnar, and E. Burkel, "Pseudo-piezoelectricity in calcium titanate—towards novel implant materials," *Scripta Materialia*, vol. 188, pp. 274-278, 2020.
- [26] J. Garay, "Current-activated, pressure-assisted densification of materials," *Annual review of materials research*, vol. 40, pp. 445-468, 2010.

- [27] R. Orru, R. Licheri, A. M. Locci, A. Cincotti, and G. Cao, "Consolidation/synthesis of materials by electric current activated/assisted sintering," *Materials Science and Engineering: R: Reports*, vol. 63, no. 4-6, pp. 127-287, 2009.
- [28] Z. A. Munir, D. V. Quach, and M. Ohyanagi, "Electric current activation of sintering: a review of the pulsed electric current sintering process," *Journal of the American Ceramic Society*, vol. 94, no. 1, pp. 1-19, 2011.
- [29] S. Jauregi, F. Fernández, R. Palma, V. Martínez, and J. Urcola, "Influence of atmosphere on sintering of T15 and M2 steel powders," *Metallurgical Transactions A*, vol. 23, no. 2, pp. 389-400, 1992.
- [30] J. G. Noudem, S. Quetel-Weben, R. Retoux, G. Chevallier, and C. Estournès, "Thermoelectric properties of  $\text{Ca}_{0.9}\text{Yb}_{0.1}\text{MnO}_{3-x}$  prepared by spark plasma sintering in air atmosphere," *Scripta Materialia*, vol. 68, no. 12, pp. 949-952, 2013.
- [31] A. Rečnik, J. Bruley, W. Mader, D. Kolar, and M. Rühle, "Structural and spectroscopic investigation of (111) twins in barium titanate," *Philosophical Magazine B*, vol. 70, no. 5, pp. 1021-1034, 1994.
- [32] V. Kodash, J. Groza, K. Cho, B. Klotz, and R. Dowding, "Field-assisted sintering of Ni nanopowders," *Materials Science and Engineering: A*, vol. 385, no. 1-2, pp. 367-371, 2004.
- [33] R. Patel, M. Patel, and A. Suthar, "Spray drying technology: an overview," *Indian Journal of Science and Technology*, vol. 2, no. 10, pp. 44-47, 2009.
- [34] N. Schell et al., "The high energy materials science beamline (HEMS) at PETRA III," in *AIP Conference Proceedings*, 2010, vol. 1234, no. 1: AIP, pp. 391-394.
- [35] N. Schell, A. King, F. Beckmann, T. Fischer, M. Müller, and A. Schreyer, "The high energy materials science beamline (HEMS) at PETRA III," in *Mater. Sci. Forum*, 2014, vol. 772, pp. 57-61.
- [36] M. Wojdyr, "Fityk: a general-purpose peak fitting program," *Journal of Applied Crystallography*, vol. 43, no. 5-1, pp. 1126-1128, 2010.
- [37] H. Rietveld, "A profile refinement method for nuclear and magnetic structures," *Journal of applied Crystallography*, vol. 2, no. 2, pp. 65-71, 1969.
- [38] L. Lutterotti, S. Matthies, H.-R. Wenk, A. Schultz, and J. Richardson Jr, "Combined texture and structure analysis of deformed limestone from time-of-flight neutron diffraction spectra," *Journal of Applied Physics*, vol. 81, no. 2, pp. 594-600, 1997.
- [39] L. Lutterotti, M. Bortolotti, G. Ischia, I. Lonardelli, and H. Wenk, "Rietveld texture analysis from diffraction images," *Z. Kristallogr. Suppl*, vol. 26, pp. 125-130, 2007.
- [40] J. Yu et al., "Effects of alcohol content and calcination temperature on the textural properties of bimodally mesoporous titania," *Applied Catalysis A: General*, vol. 255, no. 2, pp. 309-320, 2003, doi: 10.1016/s0926-860x(03)00570-2.
- [41] M. D. Abràmoff, P. J. Magalhães, and S. J. Ram, "Image processing with ImageJ," *Biophotonics international*, vol. 11, no. 7, pp. 36-42, 2004.
- [42] L. Lutterotti, R. Ceccato, R. Dal Maschio, and E. Pagani, "Quantitative analysis of silicate glass in ceramic materials by the Rietveld method," in *Materials Science Forum*, 1998, vol. 278, no. 281: Aedermannsdorf, Switzerland: Trans Tech Publications, 1984-, pp. 87-92.
- [43] M. Ishfaq et al., "1.5 MeV proton irradiation effects on electrical and structural properties of  $\text{TiO}_2/\text{n-Si}$  interface," *Journal of Applied Physics*, vol. 115, no. 17, p. 174506, 2014.
- [44] S.-W. Lee, L. Lozano-Sánchez, and V. Rodríguez-González, "Green tide deactivation with layered-structure cuboids of  $\text{Ag}/\text{CaTiO}_3$  under UV light," *Journal of hazardous materials*, vol. 263, pp. 20-27, 2013.
- [45] A. Kushima and B. Yildiz, "Role of lattice strain and defect chemistry on the oxygen vacancy migration at the (8.3%  $\text{Y}_2\text{O}_3\text{-ZrO}_2$ )/ $\text{SrTiO}_3$  hetero-interface: A first principles study," *ECS Transactions*, vol. 25, no. 2, pp. 1599-1609, 2009.
- [46] K. S. Knight, "Parameterization of the crystal structures of centrosymmetric zone-boundary-tilted perovskites: an analysis in terms of symmetry-adapted basis-vectors of the cubic aristotype phase," *The Canadian Mineralogist*, vol. 47, no. 2, pp. 381-400, 2009.
- [47] W. George and R. Grace, "Formation of point defects in calcium titanate," *Journal of Physics and Chemistry of Solids*, vol. 30, no. 4, pp. 881-887, 1969.
- [48] C. Cazorla, "Lattice effects on the formation of oxygen vacancies in perovskite thin films," *Physical Review Applied*, vol. 7, no. 4, p. 044025, 2017.
- [49] B. Richter, H. Kühlenbeck, H.-J. Freund, and P. S. Bagus, "Cluster core-level binding-energy shifts: the role of lattice strain," *Physical review letters*, vol. 93, no. 2, p. 026805, 2004.
- [50] P. S. Bagus, A. Wieckowski, and H. Freund, "The contribution of lattice strain to core-level binding energy shifts in metal nanoparticles: Generality and origin of the shifts," *Computational and Theoretical Chemistry*, vol. 987, pp. 22-24, 2012.
- [51] S. Saha, T. Sinha, and A. Mookerjee, "Structural and optical properties of paraelectric  $\text{SrTiO}_3$ ," *Journal of Physics: Condensed Matter*, vol. 12, no. 14, p. 3325, 2000.
- [52] K. Momma and F. Izumi, "VESTA 3 for three-dimensional visualization of crystal, volumetric and morphology data," *Journal of applied crystallography*, vol. 44, no. 6, pp. 1272-1276, 2011.
- [53] M. Zhou, T. Bak, J. Nowotny, M. Rekas, C. Sorrell, and E. Vance, "Defect chemistry and semiconducting properties of calcium titanate," *Journal of Materials Science: Materials in Electronics*, vol. 13, no. 12, pp. 697-704, 2002.
- [54] F. Kröger and H. Vink, "Relations between the concentrations of imperfections in crystalline solids," in *Solid state physics*, vol. 3: Elsevier, 1956, pp. 307-435.

- 1 [55] U. Diebold, "The surface science of titanium dioxide," *Surface science reports*, vol. 48, no. 5-8, pp. 53-229, 2003.
- 2 [56] H. Cheng and A. Selloni, "Surface and subsurface oxygen vacancies in anatase TiO<sub>2</sub> and differences with rutile," *Physical*
- 3 *Review B*, vol. 79, no. 9, p. 092101, 2009.
- 4 [57] J. J. Brown, Z. Ke, W. Geng, and A. J. Page, "Oxygen Vacancy Defect Migration in Titanate Perovskite Surfaces: Effect of
- 5 the A-Site Cations," *The Journal of Physical Chemistry C*, vol. 122, no. 26, pp. 14590-14597, 2018.
- 6 [58] M. Calleja, M. T. Dove, and E. K. Salje, "Trapping of oxygen vacancies on twin walls of CaTiO<sub>3</sub>: a computer simulation
- 7 study," *Journal of Physics: Condensed Matter*, vol. 15, no. 14, p. 2301, 2003.
- 8 [59] L. Goncalves-Ferreira, S. A. Redfern, E. Artacho, E. Salje, and W. T. Lee, "Trapping of oxygen vacancies in the twin walls
- 9 of perovskite," *Physical Review B*, vol. 81, no. 2, p. 024109, 2010.
- 10 [60] L. Goncalves-Ferreira, S. A. Redfern, E. Artacho, and E. K. Salje, "Ferrielectric twin walls in CaTiO<sub>3</sub>," *Physical review*
- 11 *letters*, vol. 101, no. 9, p. 097602, 2008.
- 12 [61] F. J. Humphreys and M. Hatherly, *Recrystallization and related annealing phenomena*. Elsevier, 2012.
- 13 [62] F. Maglia, I. G. Tredici, and U. Anselmi-Tamburini, "Densification and properties of bulk nanocrystalline functional
- 14 ceramics with grain size below 50 nm," *Journal of the European Ceramic Society*, vol. 33, no. 6, pp. 1045-1066, 2013.
- 15 [63] K. Huang and R. Logé, "A review of dynamic recrystallization phenomena in metallic materials," *Materials & Design*, vol.
- 16 111, pp. 548-574, 2016.
- 17 [64] Y. Zhou, K. Hirao, Y. Yamauchi, and S. Kanzaki, "Densification and grain growth in pulse electric current sintering of
- 18 alumina," *Journal of the European Ceramic Society*, vol. 24, no. 12, pp. 3465-3470, 2004.
- 19 [65] S.-Y. Choi et al., "Assessment of strain-generated oxygen vacancies using SrTiO<sub>3</sub> bicrystals," *Nano letters*, vol. 15, no. 6,
- 20 pp. 4129-4134, 2015.
- 21 [66] P. A. Cox, *Transition metal oxides: an introduction to their electronic structure and properties*. Oxford university press,
- 22 2010.
- 23 [67] S. R. Moheimani and A. J. Fleming, "Fundamentals of piezoelectricity," *Piezoelectric transducers for vibration control*
- 24 *and damping*, pp. 9-35, 2006.
- 25 [68] J. Anderson and C. Eriksson, "Piezoelectric properties of dry and wet bone," *Nature*, vol. 227, no. 5257, p. 491, 1970.
- 26 [69] E. Fukada and I. Yasuda, "Piezoelectric effects in collagen," *Japanese Journal of Applied Physics*, vol. 3, no. 2, p. 117,
- 27 1964.